Published in final edited form as:
Cytometry A. 2010 November ; 77(11): 1049–1058. doi:10.1002/cyto.a.20977.

Photothermal Multispectral Image Cytometry for Quantitative Histology of Nanoparticles and Micrometastasis in Intact, Stained and Laser Burned Tissues

Dmitry A. Nedosekin[1], **Evgeny V. Shashkov**[1,2], **Ekaterina I. Galanzha**[1], **Leah Hennings**[3], and **Vladimir P. Zharov**[1,*]

[1]Phillips Classic Laser and Nanomedicine Laboratories, University of Arkansas for Medical Sciences, Little Rock, Arkansas

[2]Prokhorov General Physics Institute, Moscow, Russia

[3]Department of Pathology, University of Arkansas for Medical Sciences, Little Rock, Arkansas

Abstract

There is a rapidly growing interest in the advanced analysis of histological data and the development of appropriate detection technologies, including mapping of nanoparticle distributions in tissue in nanomedicine applications. We evaluated photothermal (PT) scanning cytometry for color-coded imaging, spectral identification, and quantitative detection of individual nanoparticles and abnormal cells in histological samples with and without staining. Using this tool, individual carbon nanotubes, gold nanorods, and melanoma cells with intrinsic melanin markers were identified in unstained (e.g. sentinel lymph nodes) and conventionally-stained tissues. In addition, we introduced a spectral burning technique for histology through selective laser bleaching areas with nondesired absorption background and nanobubble-based PT signal amplification. The obtained data demonstrated the promise of PT cytometry in the analysis of low-absorption samples and mapping of various individual nanoparticles' distribution that would be impossible with existing assays. Comparison of PT cytometry and photoacoustic (PA) cytometry previously, developed by us, revealed that these methods supplement each other with a sensitivity advantage (up to 10-fold) of contactless PT technique in assessment of thin (≤100 μm) histological samples, while PA imaging provides characterization of thicker samples which, however, requires an acoustic contact with transducers. A potential of high-speed integrated PT–PA cytometry for rapid examination of both intact and stained heterogeneous tissues with high sensitivity at the zepromolar concentration level is further highlighted.

Keywords

histology; spectroscopy; photoacoustic method; photothermal imaging; scanning cytometry; nanoparticles; spectral burning

Histopathology is the well-established tool for diagnosis of diseases and evaluation of therapeutic interventions through the microscopic examination of tissue samples taken from anatomic areas of interest. Typically, sample preparation includes surgical extraction, fixation, embedding to paraffin or freezing, sectioning, and staining of tissues with

*Correspondence to: Vladimir P. Zharov, Phillips Classic Laser and Nanomedicine Laboratories, University of Arkansas for Medical Sciences, 4301 W. Markham Str., Little Rock, AR 72205 zharovvladimirp@uams.edu.

conventional dyes or immunohistochemical labeling with specific antibodies (1). Bright-field optical microscopy is still the mainstay for examination of histological samples (2). A trained pathologist may readily reach a diagnosis based on tissue morphology or with the use of specific staining to identify tissue components. However, this remains a time-consuming and labor-intensive procedure requiring extensive training. Processing and staining, required for bright-field microscopy, may also introduce artifactual changes not present in the native tissue. Various optical and nonoptical imaging techniques have been developed to enhance histological analysis including fluorescence microscopy (3); multispectral mapping (4); stimulated fluorescence microscopy for fluorescent proteins (5); Raman spectroscopy (6); MRI (7); X-ray technique (8); TEM (9); and mass spectrometry (10,11).

Recently, the rapidly growing application of nanotechnology in biology and medicine has placed new demands on histological analysis (12). Various nanoparticles with different sizes, shapes, and composition have been developed for gene/drug delivery, diagnosis, and therapy (13–16). Before *in vivo* clinical application of nanoparticles is feasible, it is imperative to determine critical parameters such as the clearance rate, biodistribution, and acute and chronic toxicity of nanoparticles in animal models (15,16). The TEM (9), X-ray (17) and MRI (18,19) have been used for imaging of gold, magnetic, and other nanoparticles in various tissues. However, most nonoptical methods are complex techniques requiring expensive equipment and increased costs of time and labor. Some methods may be limited to assessment of a single nanoparticle type. For example, only magnetic nanoparticles may be evaluated using MRI. Optical techniques, including diffusion optical spectroscopy (20) and optical coherence tomography (21), may reveal changes in optical parameters of tissue in the presence of nanoparticles; however, imaging contrast is low with these methods. In addition, the sensitivity of scattering-based methods is much lower than that of direct absorption measurement (22) and is not sufficient for imaging of individual nanoparticles or small aggregates.

We believe that many of these limitations may be overcome by using photoacoustic (PA), and especially photothermal (PT) imaging techniques which recently were shown to demonstrate greater sensitivity and spatial resolution compared with other optical modalities (22–32). To this end, we developed PA scanning cytometry/microscopy for imaging of unlabeled melanoma cells in a thin layer of whole blood (33), label-free mapping of real melanoma metastasis at the single cell level both *in vivo* and *in vitro* in sentinel lymph nodes (SLN) at different stages of cancer progression (25,34,35), as well as detection of tumor cells molecularly targeted by conjugated nanoparticles in lymph node samples (25,35,36). The advantages of the PA method include its combination of high sensitivity with increased depth of penetration and the flexibility in sample preparation. PA imaging does not require fixation, sectioning, and staining as in conventional histology (33–38).

PT technique has higher absorption sensitivity compared with PA technique for thin samples (39,40) as in the case of conventional histological sections with thickness of 5–50 μm. The applications of PT method have been recently reported toward transparent biological samples such as individual cells (28,41,42) and some thin tissues (40); however, the use of PT method for analysis of conventional histological samples has not yet been demonstrated. Herein, we demonstrate the excellent capability of contactless high-sensitivity PT scanning cytometry/microscopy for analysis of both conventionally fixed and stained histological samples as well as fresh histological without fixation or processing.

Materials and Methods

PT Scanning Microscope–Cytometer

The PT cytometer setup (Fig. 1A) was built on the technical platform of an invert microscope (model IX81, Olympus America, Center Valley, PA), with incorporated PT, PA, fluorescent, and transmission digital microscope (TDM) modules, and a tunable laser-based optical parametric oscillator (OPO, Opolette HR 355 LD, OPOTEK, Carlsbad, CA) with the following parameters: spectral range of 410–2,200 nm; pulse width, 5 ns; pulse repetition rate, 100 Hz; line width, ~0.5 nm; pulse energy up to 2 mJ; a fluence range, $1–10^4$ mJ/cm^2; and pulse energy stability, 3–5%. Energy of each OPO pulse was controlled by energy meter (PE10-SH, OPHIR, Logan, UT). The absorbed energy of OPO laser (also referred to as pump) pulses in the sample is transformed through quick nonradiative relaxation into heat. Laser-induced temperature-dependent variations of the refractive index around absorbing zones cause defocusing (i.e., thermal-lens effect) of a collinear probe beam from continuous waves stabilized He–Ne laser (wavelength, 633 nm; power, 1.4 mW; model 117A, Spectra-Physics, Santa Clara, CA). The subsequent change in the beam's intensity at its center (further referred to as PT signal) is detected after passing through a pinhole by a photodiode with built-in preamplifier (PDA36A, 40-dB amplification, ThorLabs, Newton, NJ). Thus, PT cytometry method is based on time-resolved optical probing of temperature gradient dynamics in the sample (e.g., cells or nanoparticles) on exposure to pump laser. The analytical signals correlate with local light absorption of the sample in the irradiated (detection) volume. In a linear mode (i.e., at low laser fluence), the observed PT signals demonstrated a fast rise (nanosecond scale) associated with quick transformation of absorbed energy into heat and a longer (microsecond scale) exponential decrease corresponding to cooling of samples through diffusion of heat into surrounding medium. At high laser fluence, sample overheating can lead to formation of nanobubbles and microbubbles around strongly absorbing zones. These nonlinear phenomena have been manifested through appearance of a negative sharp peak in PT signals due to refraction and scattering phenomena in rapidly (~0.5 to 2 μs) expanding and collapsing bubbles (Fig. 1A, right top). PT imaging (PTI) mode was provided by scanning samples with a two-dimensional (2D; *X*–*Y*) translation stage (H117 ProScan II, Prior Scientific, Rockland, MA) having positioning accuracy of 50 nm. The intensity of each pixel of PT image represents the average of PT signals (averaged absolute values of probe beam intensity change) from several OPO pulses (Fig. 1A, right bottom). The ultimate lateral resolution of PTI was determined by the focal spot size of the pump laser beam. For micro-objectives with magnification of 20× (NA 0.45) and 100× (NA 1.25), spatial resolution was estimated as ~1.0 μm and ~0.5 μm, respectively (for excitation wavelength of 740 nm).

A color CCD camera (PC135C-4G, Supercircuits, Austin, TX) was used to track positions and dimensions of the laser beams in the sample plane. Conventional absorption spectra were obtained by spectrophotometer (USB4000, Ocean Optics, Dunedin, FL) collecting transmitted light through an ocular via custom-made fiber connector.

A PC (Dell Precision 690) equipped with a high-speed (200 MHz) analog-to-digital converter board PCI-5124, 12-bit card, 128 MB of memory (National Instruments, Austin, TX) was used to acquire PT signals. Synchronization of the pump laser, signal acquisition/procession, and control over translation stage were implemented in a single software module (customized software based on LabView 8.5 complex, National Instruments).

Nanoparticles

Single-walled carbon nanotubes (CNTs) with an average length and diameter of 190 nm and 1.7 nm, respectively, were purchased from Carbon Nanotechnologies (Houston, TX).

Ultrasonic cleaner (Branson 2200, Branson Ultrasonic, Danbury, CT) was used to disperse large CNT aggregates. CNT solution typically contained both individual nanoparticles and aggregates. The average size of aggregates in the solution was controlled by high-resolution optical imaging with 100× microobjective. Depending on the duration of ultrasonic treatment and filtering procedure, the average aggregate sizes could be selected in the broad range of 0.3–10 μm. Gold nanorods (GNRs) with axial size 30 nm, diameter 10 nm, peak absorption at 740 nm were purchased from Nanopartz (Loveland, CO).

Animal Model, Cells, and Histological Procedures

Nude mice weighing 20–25 g (Harlan Spraque-Dawley) were used in accordance with protocols approved by University of Arkansas for Medical Sciences Institutional Animal Care and Use Committee. B16F10 mouse melanoma cells were obtained from a cell bank (American Type Culture Collection). Melanoma cells (10^6 B16F10 cells in a 50-μL suspension) were inoculated subcutaneously in the mouse ear. Distribution of CNTs in histological samples was studied on melanoma-bearing mice. Selected mice were used to determine the ability of PTI to detect micrometastatic lesions.

First model was created by injection of CNTs in a phosphate-buffered (PBS) solution (2.5 μg delivered in 50 μL of PBS) into the tail vein 4 days after melanoma implantation. A complete necropsy was performed at 23 days post-CNT injection. The spleen, kidney, liver, lung, lymph nodes, and heart were fixed in 10% neutral buffered formalin, processed and embedded into paraffin, sectioned at 5 μm, and mounted onto microscope slides. Slides were stained with hematoxylin and eosin (H&E) dye, and a serial section from each slide was left unstained. To differentiate CNTs from melanin, slides containing CNTs were subjected to melanin chemical bleaching in 1% potassium permanganate solution for 30 min followed by washing in PBS and decolorization with 2% oxalic acid. After bleaching, samples were stained with H&E and examined by PT and optical microscopes.

Second model was created by allowing tumors in mice to grow for 7 and 14 days, respectively, and the mice were euthanized in CO_2 chamber. Immediately following euthanasia, the SLN were extracted, washed with PBS, placed on a glass slide, and covered with a coverslip. Gentle pressure was applied to the coverslip to spread lymph node. In selected experiments glycerol was used to improve optical imaging and prevent sample drying.

Microscopic and H&E pathological examination and immunohistochemistry were carried out by a veterinary pathologist using Olympus invert IX81 microscope with digital camera (DP72, Olympus America, Center Valley, PA).

For PT cytometer calibration purposes, unstained 5-μm-thick histological sections of control mice without tumor or injected nanoparticles were spiked with GNR or CNTs nanoparticles. Samples were deparaffinizated in xylene and washed with 95% ethanol. Then, 10 μL of nanoparticle solution (10 μg/mL) was placed locally on the surface of deparaffinized tissues for 30 s. Non-adhered nanoparticles were removed by three washings in PBS. Glycerol was topically applied on the sample surface to improve imaging quality, and then samples were sealed with a coverslip.

Results

PTI of Stained Tissue Samples

PT mapping was provided by successive monitoring of PT signals during movement of a microscopic stage with the sample at the fixed position of the focused laser beam (Fig. 1A); color-coded scale is used to represent PT signal amplitude. For validation of PT mapping

accuracy and resolution, we selected dyes used in routine histology. Hematoxylin is a blue–purple, basic dye that stains regions rich in nucleic acids, i.e. ribosomes, chromatin-rich cell nucleus, and some cytoplasmic regions (1). Alcohol-based acidic eosin Y stains intracellular or extracellular proteins in bright pink color. The absorption spectra of dyes are partially overlappping (Fig. 1B). PT signal amplitude is proportional to a total light absorption of the sample; thus, amplitude in each image pixel at eosin absorption maximum wavelength (~530 nm) represents the sum of absorption from both the dyes (Fig. 2A, right). At 625 nm (hematoxylin maxima–eosin minima), PT signal was preferentially determined by hematoxylin content (Fig. 2A, middle). In general, PT images demonstrate high sensitivity, high resolution, and high contrast.

To demonstrate spectral selectivity of PT cytometry in imaging mode, we examined melanoma cells in distant meta-static sites of tumor-bearing mice. Melanin is an intrinsic marker distinguishing malignant melanoma metastasis (34). Melanin has wide absorption spectra with gradual, slight decrease in absorption with increasing wavelength (Fig. 1B). Selective detection of melanoma cells was performed at OPO wavelength of 800 nm, where influence of H&E stain is minimal. PT mapping clearly indicated the presence of melanin in tissues with metastasis (Fig. 2B). Indeed, PT image sensitivity and contrast were high enough to distinguish small melanin inclusions in melanin-containing cells not visible by optical transmission microscopy (Fig. 2B, enlarged parts). The melanin detection limit at the laser fluence used was estimated as a single melanin particle with a size of 0.9 ± 0.2 μm in the 3-μm laser spot. Thus, presence of intensive PT signals reveals presence of melanin in tissues and could be used to identify metastatic melanoma. Comparison of melanin content in metastatic and healthy tissues could be used for quantitative analysis based on an average PT signal for a given area of the sample. For tissue sample considered herein (Fig. 2B, enlarged part), with low melanin content, PT signal averaged over 60×60 μm^2 area was $(43 \pm 4) \times 10^{-2}$ a.u. that significantly differs from an average PT signal of healthy tissues $(5 \pm 0.4) \times 10^{-2}$ a.u. ($n = 360$, $P = 0.95$; Fig. 2B). Quantification of melanin content in tissues may be useful for detection of the very early metastasis before morphological changes become readily visible in H&E stained sections.

PT Spectral Analysis with Spectral Burning Techniques

PT spectroscopy represents an additional mode of PT cytometer for sample characterization through spectral identification of the individual components in the spectral range of OPO (410–2,200 nm). By acquiring PT signal amplitudes at different OPO wavelengths, we obtained PT spectra from local areas (Fig. 3B) that correlated well with conventional absorption spectra (Fig. 3A). Both PT and absorption spectra represent sum of H&E dyes in the sample as mentioned above. For example, for the tissues reacting with eosin (pink), eosin band prevailed both in PT and absorption spectra (Figs. 3A and 3B: I, II, and IV). For tissues stained in the blue–purple range, PT and absorption spectra reveal both H&E bands (Figs. 3A and 3B: III and V). PT spectra of metastatic melanoma cells (Fig. 3B: VI) corresponded well to the conventional absorption spectrum of melanin (Fig. 1B).

Next, we studied PT signal behavior as a function of pump laser fluences. PT signal linearly depended on pump pulse fluence at relatively low laser pulse fluence below 400 mJ/cm^2 (Fig. 4A). At this fluence, there were no signs of sample photodamage. The reproducibility of PT signals in this fluence range was relatively high with standard deviation of 3–5% for three consecutive scans. At higher laser energy above 1.0 J/cm^2, strong nonlinearity in PT signal amplitude was observed due to overheating of the irradiated volume. In particular, for energy fluence of 1.5 J/cm^2, the PT signal amplitude increased 5–10 times compared with the one at fluence of 1.0 J/cm^2 (Fig. 4A). This signal enhancement was accompanied by the appearance of nonlinear PT signals with negative amplitude (Fig. 1A, right top). This phenomenon is explained by overlapping of nano- and micro-bubbles from multiple

overheated nano- and micro-scaled heterogeneous absorbing zones in the irradiated volume, acting as PT signal amplifier (43).

Bleaching of stained samples was observed as a result of prolonged laser exposure (more than 100 laser pulses) at energy fluence exceeding 0.4 J/cm^2 for eosin at 532 nm and at fluence of 1.7 J/cm^2 for hematoxylin at 625 nm. Thus, relatively high pulse energy fluence provided both PT signal amplification and dye bleaching. This made it possible to spectrally selective "erase" one stain without bleaching of another one (Fig. 4B). This spectral PT bleaching (also referred to as laser burning) could be used to reveal weak staining in the presence of nondesired intensive background staining (Figs. 4C and 4D). A measurement of PT spectra allowed verification and real-time monitoring of laser-based hematoxylin PT bleaching with eosin remaining intact (Fig. 4B).

PT Mapping of Nanoparticles Distribution in Histological Samples: A Model Study

To assess performance of PT cytometry to nanomedicine-related applications, we used a model tissue slice spiked with nanoparticles. Nanoparticles were deposited from solution onto the surface and into the intercellular spaces of the 5-μm-thick deparaffinized tissue section. We used two types of nano-particles to validate PT mapping sensitivity: CNTs and GNRs that are both prospective PT/PA contrast agents, for which, toxicity should be assessed before clinical use (44–47). CNTs absorb light in a wide spectral range from visible to infrared with a slight gradual decrease of absorption with wavelength increased. The absorption of GNRs is more specific in near-infrared range with profound maximum at 740 nm. CNTs have a tendency to aggregate forming typical CNT clusters up to 300–500 nm, which can be distinguished and hence verified by conventional TDM. GNRs can also form aggregates; however, these aggregates were small enough that visualization by TDM was difficult.

First, we used histological samples spiked with CNTs. These samples contained a few large CNT clusters with diameter ranging from 1 to 4 μm. TDM (Fig. 5A) was used to verify result of PT detection (Fig. 5B). CNT aggregates were successfully imaged in the tissue (Fig. 5C). However, the PT data revealed numerous PT signals coming from sample areas where TDM did not reveal the presence of nanoparticles. We assume that these signals come from individual CNTs as the level of these signals significantly exceeded background level of control sample treated with PBS solution. Additionally, PT spectra from these areas were acquired to verify the nature of these signals. Obtained PT spectra were similar to conventional absorption spectra of CNTs (Fig. 1B). With the size of CNT cluster determined by high-resolution TDM, we obtained the calibration graph for PT signal as a function of cluster size (Fig. 5D). For the PT microscope configuration used, linear calibration estimates the limits of detection at the level of 200–250 nm sized cluster. However, this data requires additional verification.

Second, we tested the sensitivity of PT cytometry using samples spiked with well-sonicated CNT solution containing submicrometer clusters. Average size of each cluster was in the range of 400–800 nm as verified by high-resolution TDM (Fig. 5E). PT images had high contrast even for these small nanoparticles with a typical signal-to-noise ratio of 10 and better (Fig. 5F). We determined that the demonstrated sensitivity could be further increased more than 10-fold by increasing laser pulse energy (e.g., from 0.1 to 2.0 J/cm^2) or by decreasing detection volume with laser beams focusing to the diffraction limit. For the unstained tissues, there were no signs of laser-induced photodamage at energy fluence up to 10.0 J/cm^2 at the used wavelength of 740 nm.

For samples spiked with GNRs, we observed relatively homogeneous distribution of nanoparticles (Fig. 5H) deposited on the tissue surface (Fig. 5G). No traces of GNRs in the

sample were noted by TDM (not shown) due to low absorbance of the GNRs. Given that amplitudes of PT signals from GNRs (laser fluence of 2.0 J/cm^2) and from 5–10 μm clusters of CNTs (laser fluence of 0.1 J/cm^2) had the same level, we suppose, that total light absorbance of individual GNRs or its small clusters (100–200 nm) in the irradiated volume was smaller than that of 5 μm CNT aggregates. Thus, despite stronger absorption of individual GNRs compared to that of individual CNTs, the capability of CNTs to create large clusters provides more enhanced PT signal amplification.

PT Mapping of Carbon Nanotubes in Tissues of Mice with Melanoma

To verify our technique *in vivo*, we used B16F10 melanoma-bearing mice exposed to CNTs solution through intravenous tail injection. By selecting this model, we constructed a complex model containing not only CNTs but also metastatic melanoma cells. This model was also relevant to PT therapy of metastatic cells targeted by absorbing nanoparticles (34). Conventional histological examination at 23 days post-CNT injection demonstrated the presence of large CNT aggregates in mouse tissues. CNTs were located within the alveolar septa (Fig. 6A) and small arteries (Fig. 6B) within the lung, in Kupffer cells in the liver (Fig. 6D), and in an artery in the heart (Fig. 6E). In addition, CNTs were occasionally located within pulmonary metastases (Fig. 6C). No inflammatory infiltrates or other signs of tissue damage were found in association with CNTs. In melanoma-containing tissues, we performed melanin chemical bleaching to differentiate black CNTs from similarly colored melanin (Fig. 6C). This bleached melanin to a light brown color, while CNTs remain black.

Next, we used PT mapping to verify the nature of black material observed in the sample. Large black clumps observed in tissues provided high PT signal at the level comparable to that of CNTs in the model tissue spiked with CNTs. Increase in PT signal amplitudes with a decrease of irradiation wavelengths correlates to absorption spectrum of CNTs (Fig. 1C), which likely confirms the CNTs as main source of PT signals. On the basis of the results of PT sample mapping, we also found a number of smaller CNT clusters undetected with TDM. Several clusters with sizes around 1.5–2 μm were observed among the liver cells (Fig. 6F) despite the high background absorption of H&E stain in visible range.

PT Scanning Cytometry of Sentinel Lymph Nodes

Finally, we used PT scanning cytometer/microscope for examination of the excised tissue sample without any fixation or processing. Recently, we reported the use of PA scanning cytometry of the SLN to detect and map metastatic melanoma cells (34). On the basis of this experience, similar animal models, and the same protocols (34), we provided PT assessment of the SLN extracted from melanoma-bearing mice. Light scattering was decreased and imaging quality improved by immersion of the tissue into glycerol. The SLNs were additionally slightly squeezed between glass slides (Figs. 7C and 7D). SLNs were analyzed using the same method as conventional histological samples. PT mapping revealed the presence of intensive PT signals in SLNs at both 7 and 14 days post tumor inoculation (Figs. 7A and 7B). PT images showed the presence of micrometastases at the first week that significantly increased at the second week. Primary tumor sizes at weeks 1 and 2 were 1.2 ± 0.3 mm^2 and 4.0 ± 0.8 mm^2, respectively. There were no PT signals above background level recorded from SLN of a control healthy mouse with no tumor melanoma implanted. These data were well correlated with the results obtained with PA scanning cytometry (34). In particular, no sign of metastasis was found with conventional histological assays after 7 days. This suggests that both PT and PA techniques allow label-free detection of early micrometastases (after first week) at single cell level, which cannot be achieved by conventional assay. Moreover, in this case optimal conditions for quantification of light absorbing component are provided as no fixation or tissue procession is required (48).

Discussion

To our best knowledge, this is the first demonstration of the use of pump-probe PT thermal lens method for examination of real histological samples. PT technique was validated for imaging and quantification of stains in a tissue sample, mapping of melanin content in melanoma metastasis, assessment of model samples spiked with CNTs and GNRs, and eventual detection of CNTs in mouse histological tissue sections after intravenous injection of CNTs. Our data indicate that sensitivity of the PT method is sufficient to detect individual melanoma cells even with very low melanin content as well as to detect individual submicrometer sized nanoparticle clusters. We were also able to demonstrate PT spectral identification of individual nanoparticles that were not visible with conventional assays in tissue sections. Integration of PT scanning image cytometry, PT spectroscopy, and conventional optical bright-field TDM microscopy provided opportunity for detailed observation of morphological tissue features and ultra-high sensitivity detection, quantification and spatial localization of nanoparticles. No additional sample preparation is required for PT analysis of histological samples; moreover, high PT contrast allows nondestructive mapping of a wide range of nanoparticles in the sample without the need for enhancement of nanoparticle optical properties [e.g., with silver staining kit (49) used to image gold nanoparticles].

Given the extremely fast growth in a number of nanotechnology applications in biology and medicine, we expect wide range of PT cytometry applications including detection of various types of light-absorbing nanoparticles such as gold nanoparticles or quantum dots (29). Besides biodistribution of nanomaterials in different tissues, possible applications could include study of cell-nanoparticle interaction, verification of the relationship between morphological tissues changes and presence of nanoparticles with a focus on acute and long-term toxicity. Routine detection of nanoparticles in histological sections via conventional methods is challenging (see Introduction Section), and in samples with a low density of nanomaterials, many sections must be examined at high magnification and/or with the use of enhancing kits. PT technique may reduce analysis duration providing rapid examination with higher sensitivity compared with existing assays. Our data demonstrates that in current configuration detection limits for CNTs were at the level of individual 150–200 nm nanoparticle clusters in the detection volume with potential for detection of single nanoparticles.

We also consider PT cytometry as a tool for verification and refinement of conventional histopathology data. First, PT contrast superior to that of conventional optical microscopy could be used for detailed analysis of weakly stained histological structures. We expect significant increase in the amount of information acquired from low contrast or weak stains in immunohistochemistry with the use of PTI and functionalized nanoparticles (to be addressed in our future study). We recently demonstrated the unprecendented high sensitivity of PT cytology in detection of small amounts of antibody-nanoparticle conjugates bound with specific antigens of breast cancer cells (36). The same protocol can be applied for PT cytometry of histological tissue sections. Second, PT analysis is capable of localizing and quantifying label-free subcellular molecular chromophores. As we demonstrated previously (28), sensitivity of pulsed PT method is sufficient for mapping low amount (up to 15 zeptomol) and distribution of intrinsic cell chromophores such as cytochrome *c* in unstained cells. This methodology could be easily extended to histological samples. Third, the observed effects of dye PT bleaching under intensive laser irradiation may become a powerful tool for identification of weakly absorbing components (50) against strongly absorbing nondesired background by selective laser-based photobleaching of the stains in the sample. In this case, the PT technique simultaneously erases nondesired dye and controls amount of the remaining dye through acquiring PT signals. A similar approach was reported

for fluorescent labeling of proteins in tissue samples (51) and for cells in microarray (52); nevertheless, to the best of our knowledge, controllable laser-based erasing of nondesired background stains in histological samples was proposed here for the first time.

Previously reported application of PA scanning cytometry for early detection of metastasis in nonstained biopsy samples of SLNs (34) was herein repeated by PT assessment of the extracted SLNs. Comparison of these approaches demonstrated the complementary nature of PA and PT scanning cytometry technologies: in combination, these methods may cover a wider range of tissue samples and provide more detailed information than if used alone. The advantage of PA cytometry is the ability to image relatively thick samples, while contactless PT cytometry provide higher sensitivity (10–50 folds) for samples less than 120-μm thick. It should be noted that PT and PA methods are based on similar physical processes (optical excitation → nonradiative relaxation → medium heating → detection of thermal-based effects) and both methods target objects with similar properties (absorbing or weekly fluorescent objects). Both may be used for many applications in spectroscopy, microscopy, analytical chemistry, and biomedicine. The difference between the methods is the detection parameter [thermal generation of acoustic waves (PA) or temperature-dependent changes in refraction index (thermal lens, PT)]. The laser-induced temperature profile in the sample could be detected by various methods: thermometry, infrared radiometry, deflection, phase contrast, polarization interference contrast, heterodyne, acoustic, and other schematics (22–25,32,34,39,42). Detection parameters influence detection schematics, creating advantages and limitations for each method. For example, in PA methods, the ultrasound transducer must be in acoustic contact with samples, while in contactless PT thermal lens method, the distance between photodetector and sample can be tens of centimeters.

The relative ease of use of the PT/PA-based methods and lack of additional histological sample preparation (including staining free analysis) provide key advantages of these methods over other optical modalities. The nanosecond laser-based pump-probe thermal lens schematic used in this work has rather simple optical scheme, is robust, and allows detection sensitivity sufficient for nanoparticles [pump-probe thermal lens method sensitivity is less affected by light scattering than that of conventional spectrophotometry or scattering-based PTmethods (22,39)].

For the current setup with OPO operating at 100-Hz pulse rate, PT mapping of the sample area of 100 × 100 μm^2 with 1-μm resolution took at least 3.2 min (total time per pixel was defined by translation stage response time of 20 ms). These parameters can be significantly improved using advanced optical components and lasers. In particular, a short PT/PA signal duration of 2–10 μs in the time-resolved mode could be used for rapid (millisecond scale) examination of histological samples using pulsed nanosecond laser with high pulse rates (up to 100–500 kHz; 53). In this case, high pulse rate allows the use of high-speed mechanical stage operating at linear rate of up to 10 cm/s, while maintaining 1-μm PT/PA image resolution. This scheme could be preferred for large sample areas with fast linear sweeps over the sample surface. On the other hand, for relatively small areas, a 2D PT/PA imaging with the use of an advanced scanning system (54) could acquire PT images containing 10 × 10 (one cell) or 100 × 100 pixels in 1 and 100 ms, respectively (100-kHz laser source, one laser pulse per pixel). The PT schematic could be easily integrated into different microscope systems.

With the current schematic, the PT image is correlated with a 2D depth-integrated absorption distribution in the irradiated volume. High sensitivity of PT/PA technique may provide assessment of weakly absorbing samples that is unachievable with other optical modalities. Further development of the technique could include 3D PT mapping of tissues with confocal PT microscopy (55), PT tomography as analogous to PA tomography

(31,32,56), far-field PT microscopy beyond diffraction limit (57), and fast scanning imaging with a high pulse rate laser (53). It would be intriguing to combine PT, PA, optical, and fluorescent imaging modalities in a single universal multifunctional setup to increase the range of detectable substances, sensitivity, specificity, and allow for flexible analysis of tissue samples of various thickness.

Acknowledgments

Grant sponsor: National Institutes of Health; Grant numbers: R01EB000873, R01CA131164, R01EB009230, and R21CA139373; Grant sponsor: National Science Foundation; Grant number: DBI-0852737.

Literature Cited

1. Greep, RO.; Weiss, L., editors. Histology. McGraw-Hill; New York: 1977.
2. Pertsinidis A, Zhang Y, Chu S. Subnanometre single-molecule localization, registration and distance measurements. Nature. 2010; 466:647–651. [PubMed: 20613725]
3. Scivetti M, Lucchese A, Ficarra G, Giuliani M, Lajolo C, Maiorano E, Favia G. Oral pulse granuloma: Histological Findings by confocal laser scanning microscopy. Ultra-struct Pathol. 2009; 33:155–159.
4. Boucheron LE, Bi ZQ, Harvey NR, Manjunath BS, Rimm DL. Utility of multispectral imaging for nuclear classification of routine clinical histopathology imagery. BMC Cell Biol. 2007; 8:S8. [PubMed: 17634098]
5. Min W, Lu SJ, Chong SS, Roy R, Holtom GR, Xie XS. Imaging chromophores with undetectable fluorescence by stimulated emission microscopy. Nature. 2009; 461:1105–1109. [PubMed: 19847261]
6. Hutchings J, Kendall C, Smith B, Shepherd N, Barr H, Stone N. The potential for histological screening using a combination of rapid Raman mapping and principal component analysis. J Biophotonics. 2009; 2:91–103. [PubMed: 19343688]
7. Meadowcroft MD, Zhang ST, Liu WZ, Park BS, Connor JR, Collins CM, Smith MB, Yang QX. Direct magnetic resonance imaging of histological tissue samples at 3.0T. Magn Reson Med. 2007; 57:835–841. [PubMed: 17457873]
8. Zehbe R, Haibel A, Riesemeier H, Gross U, Kirkpatrick CJ, Schubert H, Brochhausen C. Going beyond histology. Synchrotron micro-computed tomography as a methodology for biological tissue characterization: From tissue morphology to individual cells. J R Soc Interface. 2010; 7:49–59. [PubMed: 19324670]
9. Lin P, Chen J-W, Chang LW, Wu J-P, Redding L, Chang H, Yeh T-K, Yang CS, Tsai M-H, Wang H-J, Kuo YC, Yang R. Computational and ultrastructural toxicology of a nanoparticle, quantum dot 705, in mice. Environ Sci Technol. 2008; 42:6264–6270. [PubMed: 18767697]
10. Schwamborn K, Wellmann A, Knuechel R, Krieg R. MALDI-imaging—A combination of histology with mass spectrometry for discovery of protein patterns with potential clinical impact. Cytometry Part A. 2007; 71A:58.
11. Kriegeskotte C, Cantz T, Haberland J, Zibert A, Haier J, Köhler G, Schöler HR, Schmidt HH-J, Arlinghaus HF. Laser secondary neutral mass spectrometry for copper detection in micro-scale biopsies. J Mass Spectr. 2009; 44:1417–1422.
12. Marquis BJ, Love SA, Braun KL, Haynes CL. Analytical methods to assess nanoparticle toxicity. Analyst. 2009; 134:425–439. [PubMed: 19238274]
13. Azzazy HME, Mansour MMH. In vitro diagnostic prospects of nanoparticles. Clin Chim Acta. 2009; 403:1–8. [PubMed: 19361470]
14. Jain KK. Applications of nanobiotechnology in clinical diagnostics. Clin Chem. 2007; 53:2002–2009. [PubMed: 17890442]
15. Clift MJ, Gehr P, Rothen-Rutishauser B. Nanotoxicology: A perspective and discussion of whether or not in vitro testing is a valid alternative. Arch Toxicol. in press [DOI: 10.1007/s00204-010-0560-6].

16. Holl MMB. Nanotoxicology: A personal perspective. Wiley Interdiscip Rev Nanomed Nanobiotechnol. 2009; 1:353–359. [PubMed: 20049802]

17. Alexiou C, Arnold W, Hulin P, Klein RJ, Renz H, Parak FG, Bergemann C, Lubbe AS. Magnetic mitoxantrone nanoparticle detection by histology, X-ray and MRI after magnetic tumor targeting. J Magn Magn Mater. 2001; 225:187–193.

18. Al Faraj A, Cieslar K, Lacroix G, Gaillard S, Canot-Soulas E, Cremillieux Y. In vivo imaging of carbon nanotube biodistribution using magnetic resonance imaging. Nano Lett. 2009; 9:1023–1027. [PubMed: 19199447]

19. Jain TK, Reddy MK, Morales MA, Leslie-Pelecky DL, Labhasetwar V. Biodistribution, clearance, and biocompatibility of iron oxide magnetic nanoparticles in rats. Mol Pharm. 2008; 5:316–327. [PubMed: 18217714]

20. Zaman RT, Diagaradjane P, Wang JC, Schwartz J, Rajaram N, Gill-Sharp KL, Cho SH, Rylander HG, Payne JD, Krishnan S, Tunnell JW. In vivo detection of gold nanoshells in tumors using diffuse optical spectroscopy. IEEE J Sel Top Quantum Electron. 2007; 13:1715–1720.

21. Kirillin M, Shirmanova M, Sirotkina M, Bugrova M, Khlebtsov B, Zagaynova E. Contrasting properties of gold nanoshells and titanium dioxide nanoparticles for optical coherence tomography imaging of skin: Monte Carlo simulations and in vivo study. J Biomed Opt. 2009; 14:021017. [PubMed: 19405730]

22. van Dijk MA, Tchebotareva AL, Orrit M, Lippitz M, Berciaud S, Lasne D, Cognet L, Lounis B. Absorption and scattering microscopy of single metal nanoparticles. Phys Chem Chem Phys. 2006; 8:3486–3495. [PubMed: 16871337]

23. Wang, LV., editor. Photoacoustic Imaging and Spectroscopy. CRC Press; Boca Raton, FL: 2009.

24. Cognet L, Lounis B. Ultra-sensitive detection of individual gold nanoparticles: Spectroscopy and applications to biology. Gold Bull. 2008; 41:139–146.

25. Kim JW, Galanzha EI, Shashkov EV, Moon HM, Zharov VP. Golden carbon nanotubes as multimodal photoacoustic and photothermal high-contrast molecular agents. Nat Nanotechnol. 2009; 4:688–694. [PubMed: 19809462]

26. Zharov VP, Mercer KE, Galitovskaya EN, Smeltzer MS. Photothermal nanotherapeutics and nanodiagnostics for selective killing of bacteria targeted with gold nanoparticles. Biophys J. 2006; 90:619–627. [PubMed: 16239330]

27. Shimizu H, Mawatari K, Kitamori T. Development of a differential interference contrast thermal lens microscope for sensitive individual nanoparticle detection in liquid. Anal Chem. 2009; 81:9802–9806. [PubMed: 19894703]

28. Brusnichkin AV, Nedosekin DA, Galanzha EI, Vladimirov YA, Shevtsova EF, Proskurnin MA, Zharov VP. Ultrasensitive label-free photothermal imaging, spectral identification, and quantification of cytochrome c in mitochondria, live cells, and solution. J Biophotonics. in press [DOI: 10.1002/jbio.201000012].

29. Shashkov EV, Everts M, Galanzha EI, Zharov VP. Quantum dots as multimodal photoacoustic and photothermal contrast agents. Nano Lett. 2008; 8:3953–3958. [PubMed: 18834183]

30. Kim C, Song KH, Gao F, Wang LHV. Sentinel lymph nodes and lymphatic vessels: Noninvasive dual-modality in vivo mapping by using indocyanine green in rats-volumetric spectroscopic photoacoustic imaging and planar fluorescence imaging. Radiology. 2010; 255:442–450. [PubMed: 20413757]

31. Razansky D, Distel M, Vinegoni C, Ma R, Perrimon N, Koster RW, Ntziachristos V. Multispectral opto-acoustic tomography of deep-seated fluorescent proteins in vivo. Nat Photon. 2009; 3:412–417.

32. Ntziachristos V, Razansky D. Molecular imaging by means of multispectral optoacoustic tomography (MSOT). Chem Rev. 2010; 110:2783–2794. [PubMed: 20387910]

33. Galanzha EI, Shashkov EV, Spring PM, Suen JY, Zharov VP. In vivo, noninvasive, label-free detection and eradication of circulating metastatic melanoma cells using two-color photoacoustic flow cytometry with a diode laser. Cancer Res. 2009; 69:7926–7934. [PubMed: 19826056]

34. Galanzha EI, Kokoska MS, Shashkov EV, Kim JW, Tuchin VV, Zharov VP. In vivo fiber-based multicolor photoacoustic detection and photothermal purging of metastasis in sentinel lymph nodes targeted by nanoparticles. J Biophotonics. 2009; 2:528–539. [PubMed: 19743443]

35. Galanzha EI, Shashkov EV, Kokoska MS, Myhill JA, Zharov VP. In vivo non-invasive detection of metastic melanoma in vasculature and sentinel lymph nodes by photoacoustic cytometry. Lasers Surg Med. 2008; s20:81.
36. Galanzha EI, Shashkov EV, Kelly T, Kim JW, Yang LL, Zharov VP. In vivo magnetic enrichment and multiplex photoacoustic detection of circulating tumour cells. Nat Nanotechnol. 2009; 4:855–860. [PubMed: 19915570]
37. McCormack D, Al-Shaer M, Goldschmidt BS, Dale PS, Henry C, Papageorgio C, Bhattacharyya K, Viator JA. Photoacoustic detection of melanoma micrometastasis in sentinel lymph nodes. J Biomech Eng. 2009; 131:074519. [PubMed: 19640155]
38. Galanzha EI, Shashkov EV, Tuchin VV, Zharov VP. In vivo multispectral, multiparameter, photoacoustic lymph flow cytometry with natural cell focusing, label-free detection and multicolor nanoparticle probes. Cytometry Part A. 2008; 73A:884–894.
39. Bialkowski, SE. Photothermal spectroscopy methods for chemical analysis. A Wiley-Interscience Publication; New York: 1996. p. 584
40. Lu SJ, Min W, Chong SS, Holtom GR, Xie XS. Label-free imaging of heme proteins with two-photon excited photothermal lens microscopy. Appl Phys Lett. 2010; 96:113701–113703.
41. Lasne D, Blab GA, De Giorgi F, Ichas F, Lounis B, Cognet L. Label-free optical imaging of mitochondria in live cells. Opt Express. 2007; 15:14184–14193. [PubMed: 19550692]
42. Tanaka Y, Sato K, Shimizu T, Yamato M, Okano T, Kitamori T. Biological cells on microchips: New technologies and applications. Biosens Bioelectron. 2007; 23:449–458. [PubMed: 17881213]
43. Zharov VP, Letfullin RR, Galitovskaya EN. Microbubbles-overlapping mode for laser killing of cancer cells with absorbing nanoparticle clusters. J Phys D: Appl Phys. 2005; 38:2571–2581.
44. Mitchell LA, Gao J, Wal RV, Gigliotti A, Burchiel SW, McDonald JD. Pulmonary and systemic immune response to inhaled multiwalled carbon nanotubes. Toxicol Sci. 2007; 100:203–214. [PubMed: 17660506]
45. Li Z, Hulderman T, Salmen R, Chapman R, Leonard SS, Young SH, Shvedova A, Luster MI, Simeonova PP. Cardiovascular effects of pulmonary exposure to single-wall carbon nanotubes. Environ Health Perspect. 2007; 115:377–382. [PubMed: 17431486]
46. Hauck TS, Ghazani AA, Chan WCW. Assessing the effect of surface chemistry on gold nanorod uptake, toxicity, and gene expression in mammalian cells. Small. 2008; 4:153–159. [PubMed: 18081130]
47. Takagi A, Hirose A, Nishimura T, Fukumori N, Ogata A, Ohashi N, Kitajima S, Kanno J. Induction of mesothelioma in p53+/− mouse by intraperitoneal application of multi-wall carbon nanotube. J Toxicol Sci. 2008; 33:105–116. [PubMed: 18303189]
48. Taylor CR, Levenson RM. Quantification of immunohistochemistry-issues concerning methods, utility and semiquantitative assessment II. Histopathol. 2006; 49:411–424.
49. Kim D, Jeong YY, Jon S. A drug-loaded aptamer-gold nanoparticle bioconjugate for combined CT imaging and therapy of prostate cancer. ACS Nano. 2010; 4:3689–3696. [PubMed: 20550178]
50. Purchase R, Volker S. Spectral hole burning: Examples from photosynthesis. Photosynth Res. 2009; 101:245–266. [PubMed: 19714478]
51. Pierre S, Scholich K. Toponomics: Studying protein-protein interactions and protein networks in intact tissue. Mol Biosyst. 2010; 6:641–647. [PubMed: 20237641]
52. Tajiri K, Kishi H, Ozawa T, Sugiyama T, Muraguchi A. SFMAC: A novel method for analyzing multiple parameters on lymphocytes with a single fluorophore in cell-microarray system. Cytometry Part A. 2009; 75A:282–288.
53. Nedosekin DA, Sarimollaoglu M, Shashkov EV, Galanzha EI, Zharov VP. Ultra-fast photoacoustic flow cytometry with a 0.5 MHz pulse repetition rate nanosecond laser. Opt Express. 2010; 18:8605–8620. [PubMed: 20588705]
54. Huo L, Xi J, Wu Y, Li X. Forward-viewing resonant fiber-optic scanning endoscope of appropriate scanning speed for 3D OCT imaging. Opt Express. 2010; 18:14375–14384. [PubMed: 20639922]
55. Zharov VP, Galanzha EI, Ferguson S, Tuchin VV. Confocal photothermal flow cytometry in vivo. Proc SPIE. 2005; 5697:167–176.
56. Zharov, VP.; Letokhov, VS. Laser optoacoustic spectroscopy. Springer-Verlag; New York: 1986. p. 327

57. Zharov VP. Far-field photothermal microscopy beyond the diffraction limit. Opt Lett. 2003; 28:1314–1316. [PubMed: 12906074]

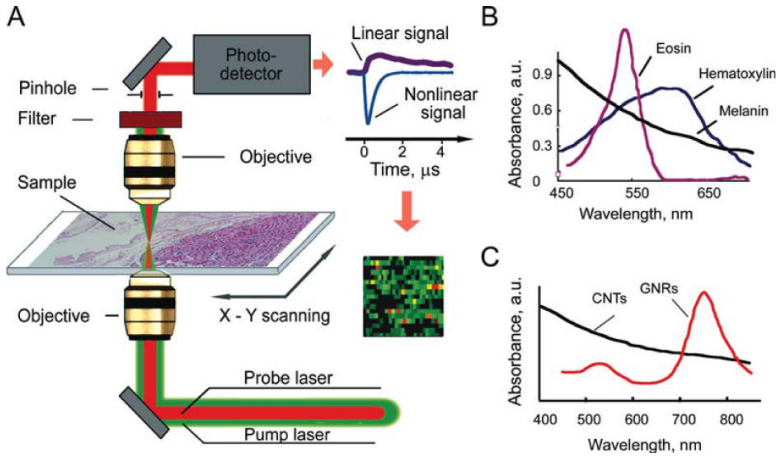

Figure 1.

PT scanning cytometry of histological samples: **A**: Schematic of PT scanning microscope-cytometer; linear and nonlinear PT signals, right top; scanning and probing sample absorbance construct color-coded PT image, right bottom; **B**: absorption spectra of melanin, eosin, and hematoxylin; and **C**: absorption spectra of carbon nanotubes (CNTs) and gold nanorods (GNRs).

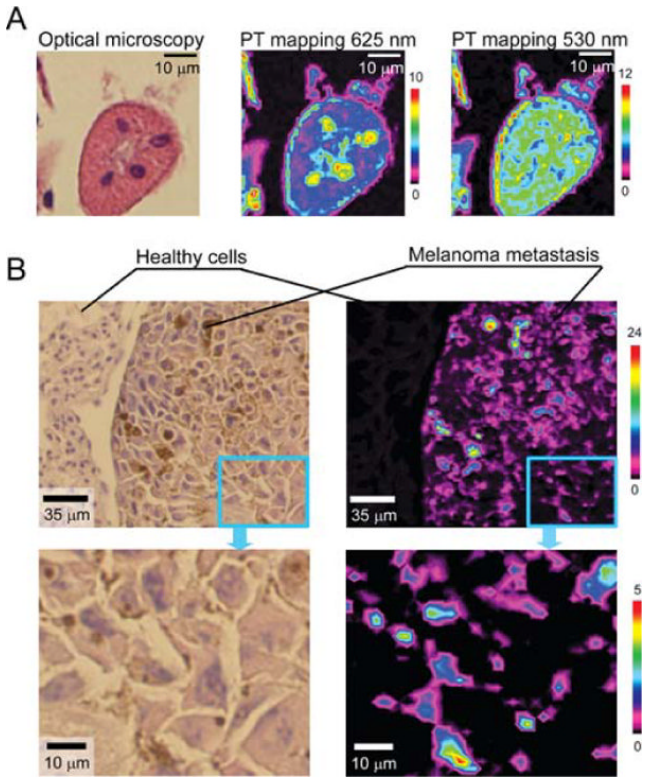

Figure 2.

PT mapping of histological sample with stains and natural chromophores (i.e., melanin). **A**: High-resolution TDM (×100 microobjective) and PT images of cells in mouse kidney tissue at OPO wavelengths 532 and 625 nm. Parameters: laser fluence, 100 and 400 mJ/cm^2, respectively; scan step, 500 nm; laser spot size, ~450 nm. **B**: Comparison of TDM and PT images of melanoma cells distribution in mouse lung with melanoma metastasis (top), the enlarged part of the images (bottom). Parameters: PT scan step, 3 μm; laser wavelength, 800 nm; laser fluence, 100 mJ/cm^2; signal-to-noise ratio, 100.

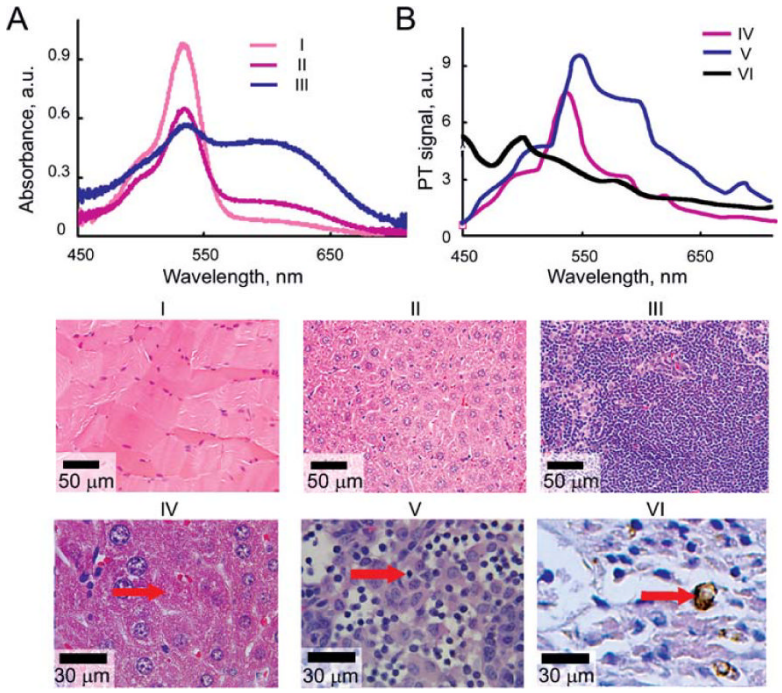

Figure 3.

Validation of PT spectral analysis: conventional (**A**) and photothermal (**B**) spectra of mouse histological samples (H&E staining): I, skeletal muscle; II and IV, liver; III and V, lymph node; and VI, melanin containing melanoma cell. Conventional spectra (A) were acquired from ~300 μm spot using fiber-coupled spectrometer. PT spectra were obtained from 3 μm spot in the sample zone denoted by red arrows. TDM images were acquired with ×40 microobjective for samples I–III and with ×100 microobjective for samples IV–VI.

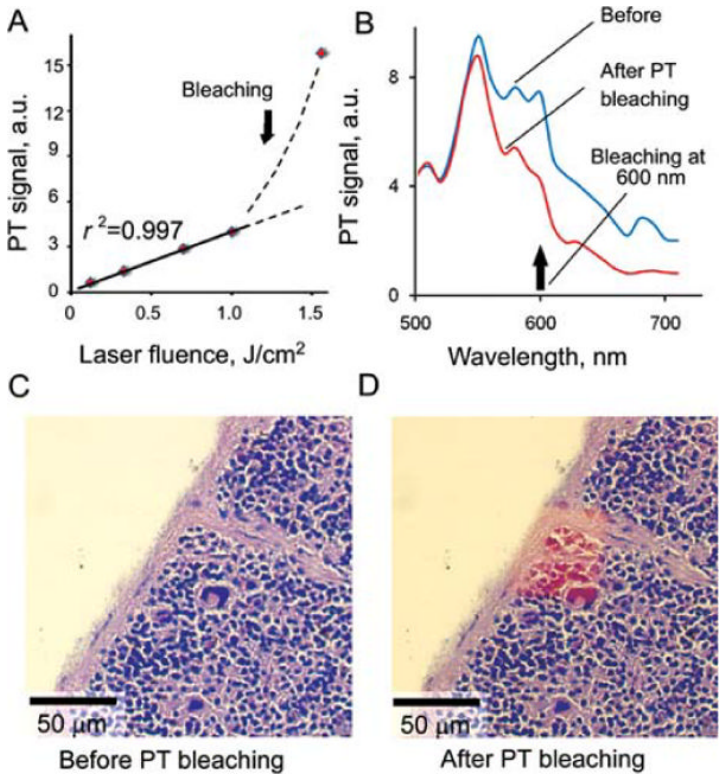

Figure 4.

Selective PT bleaching/laser burning of stain guided by PT cytometer. **A**: PT signals of hematoxylin stained sample as a function of laser fluence at wavelength of 625 nm for laser spot of 3 μm. **B**: PT spectra of mouse spleen before and after laser scanning at 625 nm at laser fluence of 2.0 J/cm^2 and 100 laser pulses per spot. TDM (optical) images of mouse spleen fragment before (**C**) and after (**D**) laser-induced PT bleaching of hematoxylin stain.

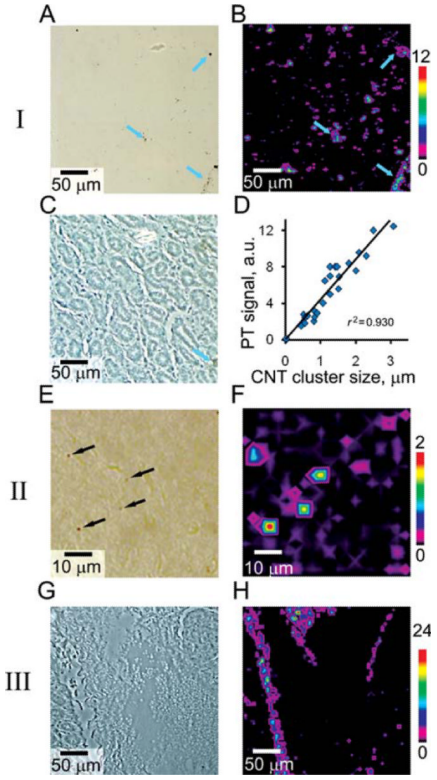

Figure 5.

PT mapping of nanoparticle distribution in model histological samples. I: CNT aggregates of 0.5–10 μm in size: TDM (**A**), PT (**B**), and phase contrast (**C**) images. Color arrows denote large aggregates presented on both images. Calibration graph (**D**) represents PT signals for clusters of different size. II: Small submicrometer sized CNT clusters: TDM image (**E**; clusters are denoted by arrows; typical size ~600–700 nm) and corresponding (**F**) PT image. III: Histological sample spiked with GNRs: phase contrast (**G**) and PT image (**H**) of GNRs distribution. Insets at right are the color scales coding amplitudes of PT signal (in au). Laser parameters: wavelength, 740 nm; pulse energy fluence, 0.1 J/cm^2 for CNTs and 2.0 J/cm^2 for GNRs; 20 signals acquired from each spot. Microscopic images (A), (C), and (G) were obtained with ×20 and (E) with ×60 microobjective.

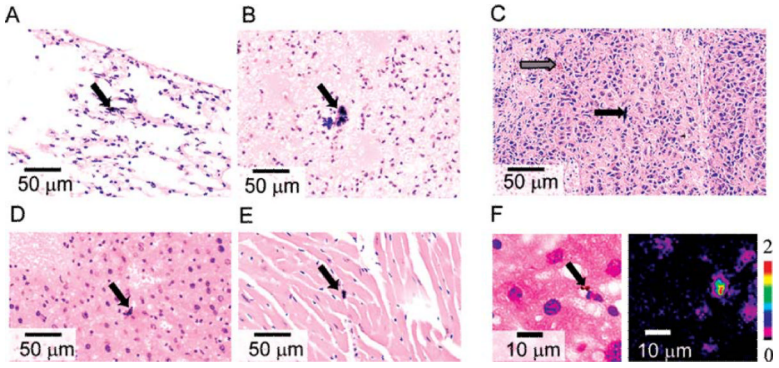

Figure 6.

Distribution of CNTs in mouse tissues. TDM images (×40 microobjective) of lung (**A, B**), liver (**D**), and heart (**E**) tissue. Differentiation of CNTs and melanin by chemical bleaching (**C**). Black arrows indicate CNTs (black color), gray arrow indicates bleached melanoma (light brown color). PT imaging reveals presence of 1.7-μm CNTs clusters in liver (**F**; ×100 microobjective). Laser parameters: wavelength, 800 nm; pulse energy fluence, 0.1 J/cm^2.

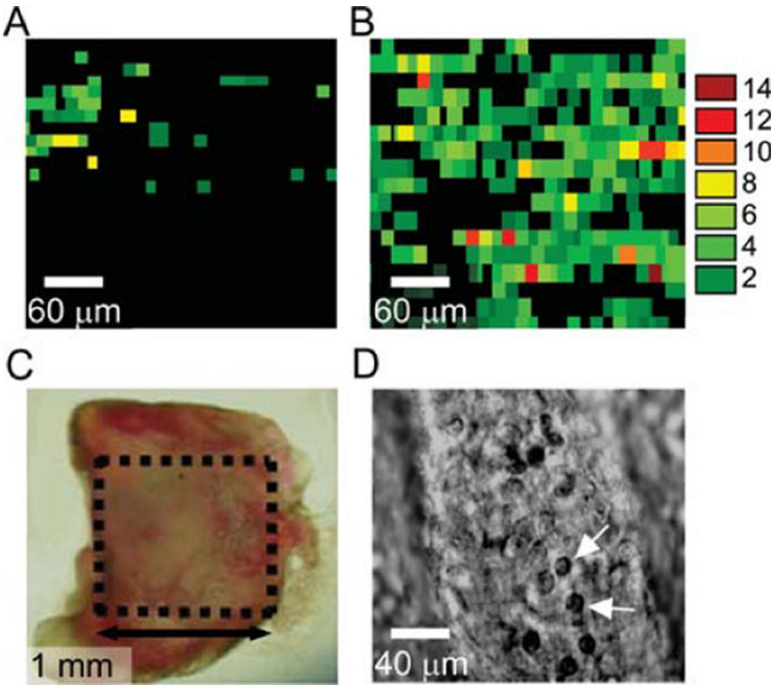

Figure 7.

Ex vivo PT mapping of metastatic melanoma cells in mouse SLNs. PT images of SLN extracted from mice at 7 (**A**) and 14 (**B**) days post inoculation. Color scale codes the amplitude of PT signals; signal of control experiment corresponds to black background. Each single color-coded pixel was associated with individual metastatic melanoma cells with different pigmentation. Laser parameters: wavelength, 850 nm; pulse energy fluence, 0.5 J/cm^2; laser spot size, 5 μm. Lymph node (**C**) was deposited on the glass slide. **D**: High-resolution TDM image of individual lymphocytes (white arrows) in the lymph node (microobjective ×100).